Appl Biochem Biotechnol (2014) 173:36–54
DOI 10.1007/s12010-014-0740-6

Biocompatible APTES–PEG Modified Magnetite Nanoparticles: Effective Carriers of Antineoplastic Agents to Ovarian Cancer

Amaneh Javid · Shahin Ahmadian · Ali Akbar Saboury · Seyed Mehdi Kalantar · Saeed Rezaei-Zarchi · Sughra Shahzad

Received: 31 October 2013 / Accepted: 10 January 2014 /
Published online: 11 March 2014

Abstract Magnetite nanoparticles are particularly attractive for drug delivery applications because of their size-dependent superparamagnetism, low toxicity, and biocompatibility with cells and tissues. Surface modification of iron oxide nanoparticles with biocompatible polymers is potentially beneficial to prepare biodegradable nanocomposite-based drug delivery agents for in vivo and in vitro applications. In the present study, the bare (10 nm) and polyethylene glycol (PEG)–(3-aminopropyl)triethoxysilane (APTES) (PA) modified (17 nm) superparamagnetic iron oxide nanoparticles (SPIO NPs) were synthesized by coprecipitation method. The anticancer drugs, doxorubicin (DOX) and paclitaxel (PTX), were separately encapsulated into the synthesized polymeric nanocomposites for localized targeting of human ovarian cancer in vitro. Surface morphology analysis by scanning electron microscopy showed a slight increase in particle size (27±0.7 and 30±0.45 nm) with drug loading capacities of 70 and 61.5 % and release capabilities of 90 and 93 % for the DOX- and PTX-AP-SPIO NPs, respectively ($p<0.001$). Ten milligrams/milliliter DOX- and PTX-loaded AP-SPIO NPs caused a significant amount of cytotoxicity and downregulation of antiapoptotic proteins, as compared with same amounts of free drugs ($p<0.001$). In vivo antiproliferative effect of present formulation on immunodeficient female Balb/c mice showed ovarian tumor shrinkage from 2,920 to 143 mm^3 after 40 days. The present formulation of APTES–PEG-SPIO-based

A. Javid · S. Ahmadian (✉) · A. A. Saboury
Institute of Biochemistry and Biophysics, University of Tehran, Tehran, Iran
e-mail: ahmadian@ibb.ut.ac.ir

S. Ahmadian
Center of Excellence of Nano-Biomedicine, Nano-Science and Nano-Technology Research Center, University of Tehran, Tehran, Iran

S. M. Kalantar
Research and Clinical Center of Infertility, Shahid Sadoughi University Medical Sciences, Yazd, Iran

S. Rezaei-Zarchi
Department of Biology, Payame Noor University, Yazd, Iran

S. Shahzad
Department of Obstetrics & Gynecology, Social Security Hospital, Islamabad, Pakistan

nanocomposite system of targeted drug delivery proved to be effective enough in order to treat deadly solid tumor of ovarian cancer in vitro and in vivo.

Keywords Salination · Ovarian cancer · Tumor volume · Cytotoxicity · Encapsulation efficiency · PEGylation

Introduction

Superparamagnetic iron oxide (magnetite, Fe_3O_4) nanoparticles (SPIO NPs) have attracted much attention because of their advantageous characteristics, such as their inertness, nontoxicity, super magneticity, ease of detection in the human body, having a magnetic core that is protected against oxidation, facilitated bioconjugating ability, catalytic surface, and potential for a variety of biological applications [1, 2]. SPIO NPs are greatly biocompatible in the human body with their ability to interact with biomolecules such as polypeptides, DNA, and polysaccharides [3]. The synthesis of biocompatible magnetite biopolymers has attracted much attention over the past several years, as they can be used in biotechnological and biomedical areas, including site-specific targeting and cancer treatment, targeted drug delivery, biodetection, and downstream processing (e.g., the purification and bioseparation of biomolecules) [4].

With a wide range of significance in the detection, diagnosis, and treatment of diseases like cancer, cardiovascular, and neurological disorders, magnetic nanoparticles may soon play a significant role in meeting tomorrow's health care needs [4–6]. As therapeutic tools, magnetic nanoparticles have been evaluated extensively for targeted delivery of pharmaceuticals through magnetic drug targeting and by active targeting through the attachment of high-affinity ligands [6, 7]. By utilizing specific targeting agents and disease biomarkers, magnetic nanoparticles offer an attractive means of remotely directing the anticancer agents specifically to the disease site while simultaneously reducing the dosage and side effects associated with the nonspecific uptake of cytotoxic drugs by healthy tissue [8].

To increase the effectiveness of magnetic nanoparticles, several techniques, including reducing the particle size and surface modification by nonfouling polymers, have been employed to improve the "stealthiness" and blood circulation time to maximize the likelihood of reaching and affecting the targeted tissues [9].

Polyethylene glycol (PEG, molecular formula $H–(OCH_2–CH_2)_n–OH$) is a high molecular weight polyether compound produced by the interaction of ethylene oxide with water, ethylene glycol, or ethylene glycol oligomers [10]. PEG is a glycol nonionic surface active agent in which the oxygen atoms are hydrophilic, while the $-CH_2-CH_2-$ displays lipophilicity. These properties have made this polymer soluble in water and most organic solvents [11]. PEG has many physical and biological properties, including hydrophilicity, dissolubility, nontoxicity, nonimmunogenicity, and no reject reactions. PEG is a classic pharmacokinetic stabilizer that has been utilized to extend nanocomposite circulation times in vivo [12]. Much to our surprise, the literature contains few reports of Magnetic nanoparticles (MNPs) primed for magnetic targeting (>100 nm, multidomain core) and shown to be sufficiently long circulating in vivo.

Intending to overcome the pharmacokinetic limitations, attributed to traditionally fast clearance, the present work aimed to produce biocompatible, controllable, agglomerate-free, and long-circulating (3-aminopropyl)triethoxysilane (APTES)–PEG (AP) modified SPIO NPs, adequate for targeted drug delivery and enhanced magnetic tumor targeting. The as-prepared drug-loaded nanocomposites were administered to human epithelial ovarian cancer cell lines of A2780 and OVCAR-3 in vitro. In addition, the anticancer effect of our drug-loaded

nanocomposites was evaluated on the ovarian cancer in vivo, after their intravenous administration to the immunodeficient cancerous mice, and their cytotoxic effects were evaluated by different techniques.

Materials and Methods

Materials

The human ovarian cancer cell lines A2780 (NCBI code, C461) and OVCAR-3 (NCBI code, C430) were purchased from Pasteur Institute, Tehran, Iran. RPMI-1640 medium and all of the additives were purchased from GIBCO Co. (Grand Island, NY, USA). Doxorubicin HCl (DOX), paclitaxel (PTX), PEG (molecular weight 2000), and APTES were purchased from Sigma-Aldrich (St. Louis, MO, USA). PEG was dehydrated under vacuum at 70 °C for 12 h and used without further purification. All other chemicals used were of highest purity and biological grade available from commercial sources.

Synthesis of PEG–APTES (Silane) Precursors

For the synthesis of PEG–APTES (AP) precursors, 30 g (6.0 mM) PEG2000 in 10 ml tetrahydrofolate (THF) was added to a solution of 864 mg (21.6 mM) NaOH in 40 ml double distilled water. The resulting mixture was stirred for 1 h at 0 °C. Then, 1.37 g (7.2 mmol) p-toluenesulfonyl chloride in 10 ml THF was added dropwise to the reaction mixture during 1 h at 0 °C and stirred for an additional 3 h. The solution was poured onto 1 M HCl, and the organic solvent was evaporated. The residue was extracted thrice with chloroform, and the organic phase was dried over $MgSO_4$, filtered. The solvent was removed by rotary evaporation. The transparent crude product, showing the substitution of terminal –OH group with Tosylate –(OTs), was used for the next step without further purification and reacted with 1.40 ml (6.0 mM) APTES in 25 ml chloroform at 70 °C for 8 h under reflux conditions, in order to bind the silane group of APTES to the PEG-OTs moiety through the amino functionality. The organic solvent was removed, and the obtained raw product was stored at 4 °C and used without further purification. In the following, the PEG–silane stoichiometry was calculated based on the total content of silane in the raw product.

Synthesis of Bare and AP-SPIO NPs

SPIO NPs were prepared using an improved chemical coprecipitation method with several modifications, resulting in substantial quality improvements. Shortly, the solutions of 5.41 g $FeCl_3 \cdot 6H_2O$ (4 ml) and 1.99 g $FeCl_2 \cdot 4H_2O$ (2 ml) were prepared in 100-ml flasks and stirred at 30 °C (pH 6.9) for 45 min. The Fe(III)/Fe(II) ratio was kept 2:1 throughout the experiment. Then, 25 ml of aqueous ammonia solution (25–28 %, w/w) was added dropwise, under the cover of N_2 gas, and the pH of the solution was carefully adjusted up to 10. The particles were filtered and rinsed with deionized water, methanol, and toluene five times in turn and dispersed in 100 ml toluene at pH 7.0.

APTES–PEGylation of SPIO NPs (AP-SPIO NPs) was done in simple fashion, using N-hydroxysuccinimide (NHS) chemistry. A 0.1-M HEPES buffer (pH 7.0) containing ~30 mg dissolved AP–NHS+10 mg SPIO NPs dissolved in 2 ml THF. The above solution was slowly added into 5 ml of deionized water under sonication at 25 °C, using an ultrasonic generator and dialyzed against deionized water for 2 days to allow the formation of hydrophilic AP-SPIO NPs and to remove organic solvents (molecular weight cut-off 50,000 Da). Afterward, the NP

solution was removed from the dialysis bag and filtered through a 0.22-μm membrane to remove large aggregates. Then, AP-modified NPs were separated by magnetic decantation with a permanent magnet. After the final wash, the purified product containing AP-SPIO NPs was concentrated to 40 mg Fe/ml.

Drug-Loaded AP-SPIO NPs

The AP-SPIO NPs (100 mg) were dispersed by sonication in 20 ml methanol containing 0.5 ml of acetic acid to form a colloid solution. DOX and PTX (1.0–250 μM, 0.1–10 mg drug/g SPIO NPs) were then separately added to the colloid solution while stirring. The high ration of drug caused it to physically diffuse into SPIO core. The solution was stirred overnight at 4 °C for 48 h to allow the partitioning of drug into NPs. The resulted drug-loaded NPs were isolated with magnet, washed with methanol until the supernatant became colorless, and dried at room temperature under vacuum. All of the supernatants were collected and diluted to 250 ml with methanol in a capacitance flask for the evaluation of drug loading efficiency by ultraviolet (UV)-visible spectrophotometry (Hitachi U-2000; λ=200–800 nm). Drug entrapment was calculated by the following formula:

$$\text{Loading efficiency } \% = \frac{[(\text{Amount of loaded drug in } \mu g)]}{[(\text{Amount of total drug added in } \mu g)]} \times 100\%$$

In Vitro Drug Release Kinetics

To study the drug release profile of DOX- and PTX-loaded AP-SPIO NPs, 3 mg of drug-loaded nanoparticles was dispersed in 30 ml of phosphate-buffered saline (PBS, pH 7.4)+ acetate buffer (pH 8.0). The pH-sensitive drug release kinetics of SPIO NPs was evaluated at the pH range of 1.5–7.4. At designated time intervals, a 3-ml sample was removed, and same volume was reconstituted by adding 3 ml of fresh PBS+acetate buffer solution to each sample. The experimental mixtures were analyzed by UV-visible spectrophotometry (200–800 nm).

Physicochemical Properties of Drug-Loaded HP-SPIO NPs

Morphological and size evaluation of the bare AP-modified and drug-loaded NPs was carried out using transmission electron microscopy (TEM, H-7600, Hitachi, 200 kV) after negative staining with uranyl acetate solution (1 % w/v). Surface characterization of all NPs was carried out using SEM. For atomic force microscopy (AFM) analysis, the HP-SPIO NPs were diluted with distilled water, and a drop of the diluents was placed on a glass plate and analyzed with AFM equipment (XE100, PSIA, Korea) in contact mode, in air. The magnetization measurements were carried out at room temperature using a vibrating sample magnetometer (VSM, Oxford Instruments, UK), with the magnetic field range of −1 to +1 Tesla (T).

Hydrodynamic diameter distribution was measured by dynamic light scattering (DLS) at 25 °C, in triplicate, from very dilute NP suspensions (1 ml) in deionized H_2O using a Zeta-Sizer instrument (DLS, Malvern Zatasizer Nano-ZS, Worcestershire, UK). The polydispersity index (PDI) was used as a measure of broadness of the size distribution.

Fourier transform infrared spectroscopy (FTIR) was used to collect infrared (IR) spectra of lyophilized samples. A 2–3-mg NP powder was mixed and ground with 100–150 mg spectroscopic-grade KBr and pressed into ~1-mm-thick disks. IR spectra were recorded using an FTIR spectrophotometer (Model 8300, Shimadzu Corporation, Tokyo, Japan) at λ=4000–400 cm^{-1}. The crystallographic state of bare AP-SPIO and drug-loaded AP-SPIO NPs was determined by X-ray diffraction (XRD, JDX-8030).

Cell Culture and In Vitro Cytotoxicity Analysis

A2780 and OVCAR-3 cells were cultured in RPMI1640 (Gibco, Invitrogen, Carlsbad, CA), supplemented with 10 % (v/v) FBS, 0.25 IU/ml insulin, 100 mg/ml streptomycin, 100 IU/ml penicillin, and 0.3 mg/ml glutamine. Cells were cultured in 96-well plates for 48 h, at a density of 1×10^5 cells/well, in a humidified atmosphere of 5 % CO_2 in air at 37 °C. The cells were then incubated with bare AP-modified, DOX-AP-SPIO, and PTX-AP-SPIO NPs at 0.1–10 μg/ml drug concentration for 96 h. After incubation completion, 10 μl of the medium containing 20 μl 3-[4,5-dimethylthiazol-2-yl]-2,5 diphenyl tetrazolium bromide (MTT) solution was added to each well, and plates were incubated for an additional 4 h, followed by the addition of 100 μl of 10 % Triton X-100+0.1 N HCl in anhydrous isopropanol (MTT solubilization solution) to each well and gently mixed to dissolve the MTT formazan crystals, and absorbance was measured with a microplate reader (Bio-Tek Instruments, Winooski, VT) at 570 nm. The background absorbance was measured at 690 nm and subtracted from the results taken from the 570-nm experiment. The cytotoxicity was expressed as the percentage of cell viability, compared with untreated control cells using the following equation:

$$\text{Viability}(\%) = \frac{N_i}{N_c} \times 100$$

Apoptotic Detection by Flow Cytometry

A2780 and OVCAR-3 cells were treated with 10 μg/ml of bare SPIO NPs, AP-SPIO, DOX-AP-SPIO, and PTX-AP-SPIO NPs in separate plates and incubated for 48 h. Apoptotic cells were identified with annexin V-FITC. Propidium iodide (PI) (BioVision, Mountain View, CA) was used according to the manufacturer's protocol to mark the dead cells. The treated cells were harvested, trypsinized, washed with PBS and incubated with annexin V-FITC and PI for 15 min at room temperature in the dark and analyzed via FACSCalibur flow cytometer with data acquisition software (CellQuest; Becton, Dickinson and Company, Mountain View, CA).

Immunoblot Analysis

A2780 and OVCAR-3 cells were lysed in a buffer containing 50 mM Tris/HCl (pH 7.4), 150 mM NaCl, 1 mM ethylenediaminetetraacetic acid, 0.2 % (v/v) Nonidet P40, and protease inhibitor cocktail in ice for a period of 10 min. Cell debris was pelleted by centrifugation, and total protein concentration of the soluble extracts was determined by Bradford assay according to the manufacturer's instructions. The survivin, Bcl-2, bax, and NF-κB proteins were separated by sodium dodecyl sulfate polyacrylamide gel electrophoresis and transferred onto nitrocellulose membranes. The enhanced chemiluminescence (ECL) detection reagent (Amersham Biosciences, USA) was used to visualize the bands. Signal intensity was determined by Quantity One version 4.6.9 for Windows.

Mouse Model: Induction of Ovarian Tumor and In Vivo Tumor Targeting

Immunodeficient BALB/c mice were a gift of Payame Noor University, Yazd, Iran, and the whole experiment was conducted according to the protocols approved by the Committee on Use and Care of Animals, Payame Noor University, Yazd, Iran. The A2780 and OVCAR-3

cells were trypsinized and resuspended in PBS buffer. The mixture containing 10^7 of both cells in a volume of 200 μl was subcutaneously injected into the peritoneal cavity of 4–6-week-old female BALB/c mice (12 mice/group) in the form of two groups: A2780 inoculated mice (A2780 group) and OVCAR-3 inoculated mice (OVCAR-3 group). Animals were kept for 30 days under controlled conditions of 14-h light:12-h dark photoperiod and fed with water and food pellets ad libitum. The mice developed tumor in one or both ovaries, intraperitoneal carcinoma, and ascites. For magnetic nanocomposite-based drug targeting, 200 μl from each of the 10 mg/ml free DOX, free PTX, DOX-AP-SPIO, and PTX-AP-SPIO NP suspensions was diluted with PBS and filtered through a 0.2-mm disposable syringe filter and separately injected to the peritoneal cavity of A2780/mice and OVCAR-3/mice (12 mice/group) and kept under above conditions for 40 days. Three mice in every group were dissected 7, 15, 25, and 40 days after the incubation, and tumor sizes were determined using the following formula:

$$\text{Tumor volume} = 0.75 \times \pi \times [\text{radius(mm)}]^3$$

Statistical Analysis

All data were presented as the mean±standard deviation (SD) unless otherwise noted. Statistical comparisons in in vitro simulations and in vivo validation studies were made using the Student's *t* test with a significance of $p<0.001$. Nonlinear regression analysis of pharmacokinetic data was performed using Excel (Microsoft, Redmond, WA).

Results and Discussion

Synthesis, Self-Assembly, and Characterization of AP-SPIO NPs

Microscopic Analysis

SPIO NPs were synthesized by chemical coprecipitation method and modified with AP. Figure 1a, b shows AFM micrographs of unmodified and AP-SPIO NPs while Fig. 1c, d shows TEM micrographs of bare and AP-SPIO NPs with 10- and 17-nm diameters, respectively. Histograms of particle size distribution (Fig. 1e, f) were obtained by image processing of the TEM micrographs by ImageJ Software and were a subsequent fit to log–normal distribution function. The estimated mean diameters of bare and AP-SPIO NPs were 10 and 17 nm, respectively (Fig. 1a–f).

Hydrodynamic Diameter Measurements

The thickness of AP coating around the SPIO NPs was characterized with DLS, which measured the hydrodynamic diameter of NPs in their dispersion state (Fig. 1g, h). The mean hydrodynamic size of unmodified and AP-SPIO NPs in distilled water was about 10 and 17 nm, respectively, indicating that magnetic cores were successfully modified with hydrophilic AP coating. As shown in Fig. 1, the APTES coating more or less directly links its amine

Fig. 1 AFM micrographs of the **a** unmodified and **b** AP-SPIO NPs. TEM micrographs of **c** unmodified and **d** ▶ AP-SPIO NPs. **e** and **f** Histograms of particle size distributions described by a log-normal distribution function for bare and AP-SPIO NPs, respectively. The histograms show the average values of 30 measurements. **g** and **h** Particle size distribution plots of unmodified and AP-SPIO NPs

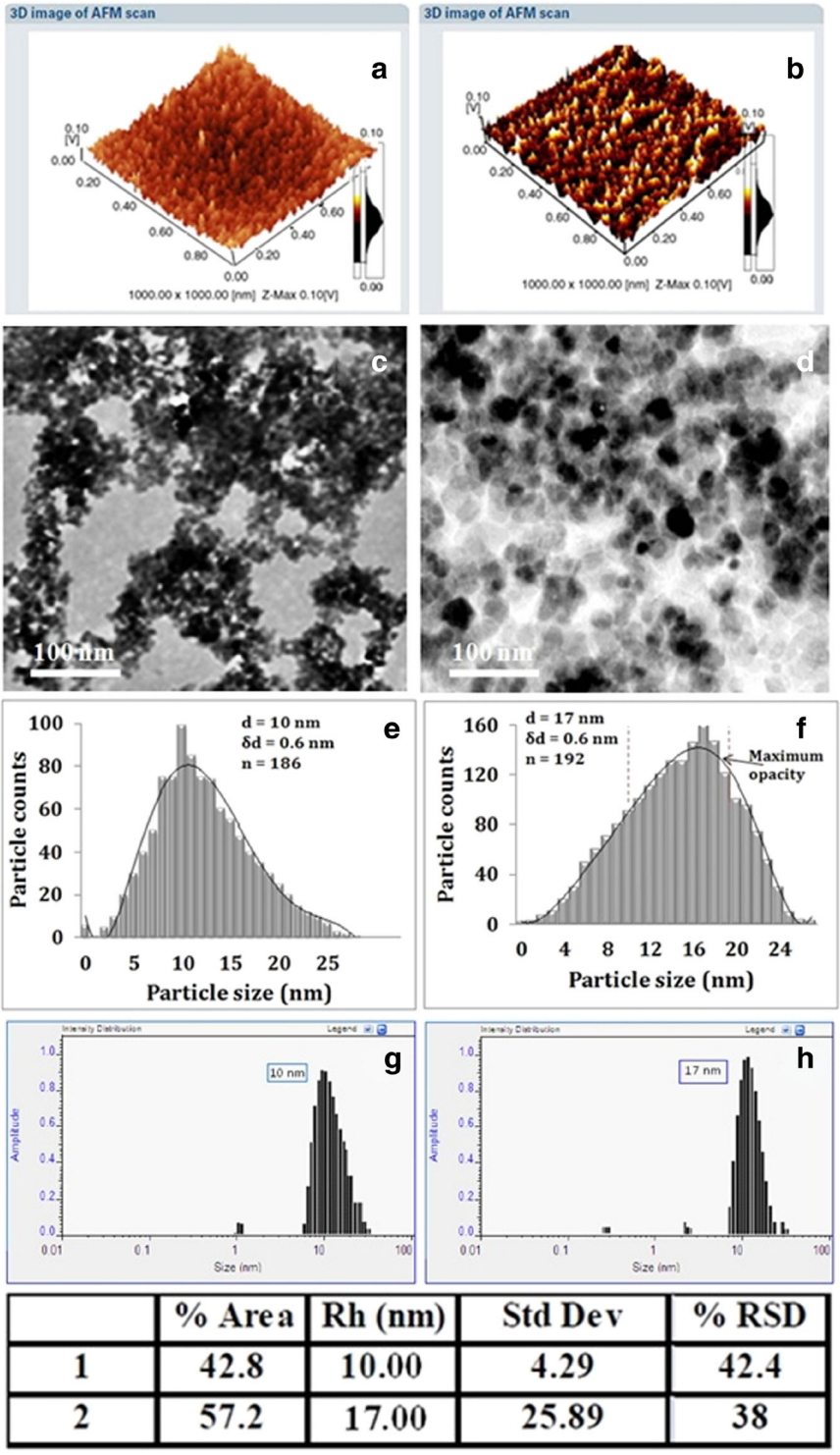

	% Area	Rh (nm)	Std Dev	% RSD
1	42.8	10.00	4.29	42.4
2	57.2	17.00	25.89	38

groups, and any cargo attached to it, to the surface of NP core via a small silica linker. These NPs were highly crystalline, uniform, and water-soluble because of the presence of amine moieties of APTES and hydrophilic methyl-polyoxyethylene amine, condensed NHS chemistry. In the PEGylated nanocomposite system, the outer PEG segment provides steric stabilization and water dispersibility to the SPIO NPs [13]. After PA modification, the nanoparticles were well dispersed in water, forming a clear solution.

FTIR Analysis

The surface modification of SPIO NPs with AP was confirmed by FTIR analysis. FTIR spectra in Fig. 2a suggest successful attachment of AP moieties to SPIO NPs. Evaluation of peaks at ~820 cm^{-1} in PEG spectra (Fig. 2a (*a*)) is the hallmark indicator of C–O–C ether bond stretching vibrations, characteristic of PEG chains [14]. Peaks of 3,450 and 3,650 cm^{-1} in spectra (*a*) and (*c*) of Fig. 2a indicate the –OH group vibrations. Spectrum (*b*) shows the Fe–O stretching vibration bands at about 590 cm^{-1}. Furthermore, new peaks at 1,575 and 1,690, due to the bending $\delta_{(NH)}$ vibration modes, appeared and replaced the characteristic peak of amino group, located at 1650 cm^{-1}, suggesting a chemical bonding between amino groups of APTES and NHS–PEG [15]. Peaks of 3,450 and 3,650 cm^{-1} in spectra (*a*) and (*c*) represent stretching vibrations of –OH groups, demonstrating that the AP was successfully coated onto SPIO NPs [16].

Magnetization Measurements

The magnetization properties of candidate AP-SPIO NPs were studied by VSM to assess the suitability of these nanocomposites for magnetic targeting. Data shown in Fig. 2b (loops (*a*) and (*b*)) indicate the magnetic properties of unmodified and AP-SPIO NPs, respectively. All candidate AP-SPIO NPs were superparamagnetic (lack of hysteresis) at room temperature and possessed similar saturation magnetization (M) around 55 emu/g Fe, which shows that the superparamagnetic property of SPIO NPs did not alter after AP modification. Ideal superparamagnetic materials should have zero coercivity and zero remanence. From the magnetization values, it can be measured that 100 % w/w AP-SPIO NPs had in fact only 23.7 % w/w AP coating on their surface [17, 18]. The inset of Fig. 2b shows the photographs of AP-SPIO NPs, dispersed in solution (left). The application of an external magnetic field (M_{ext}) to solution caused the attraction of NPs toward it, and the dispersion became clear (right-side photograph). Removal of M_{ext} and shaking caused the NPs to disperse again, which confirms that the AP-SPIO NPs were sensitive to M_{ext} and exhibited superparamagnetic property.

XRD Analysis

Nanocrystalline structure of unmodified and AP-SPIO NPs was evaluated by XRD. Figure 2c clearly indicates that the XRD patterns of bare and AP-modified NPs were similar to that of standard Fe_3O_4 structure, confirming the crystalline structure of modified NPs. The bare and AP-SPIO spectra showed approximately identical characteristic diffraction peaks at 2 =28°, 34.5°, 42.0°, 51.4°, 54.0°, and 58.8°, which corresponds to the reflection plane indices of (220), (311), (400), (511), (440), and (533), respectively, revealing that surface modification and conjugation of AP to SPIO NPs did not lead to their phase change.

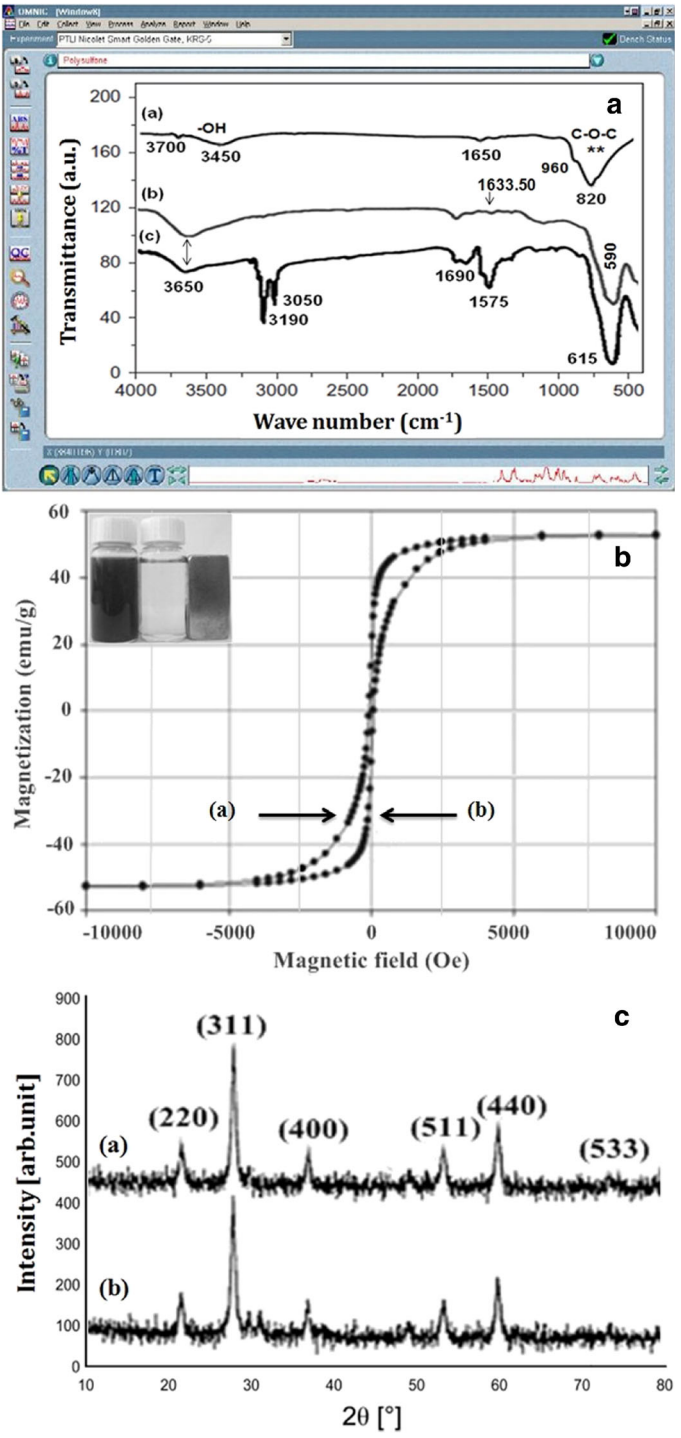

Fig. 2 **a** FTIR spectra of pure PEG (*a*), unmodified SPIO NPs (*b*), and AP-SPIO NPs (*c*). **b** Hysteresis loops of unmodified (*a*) and AP-SPIO NPs (*b*). **c** XRD patterns of unmodified (*a*) and AP-SPIO NPs (*b*)

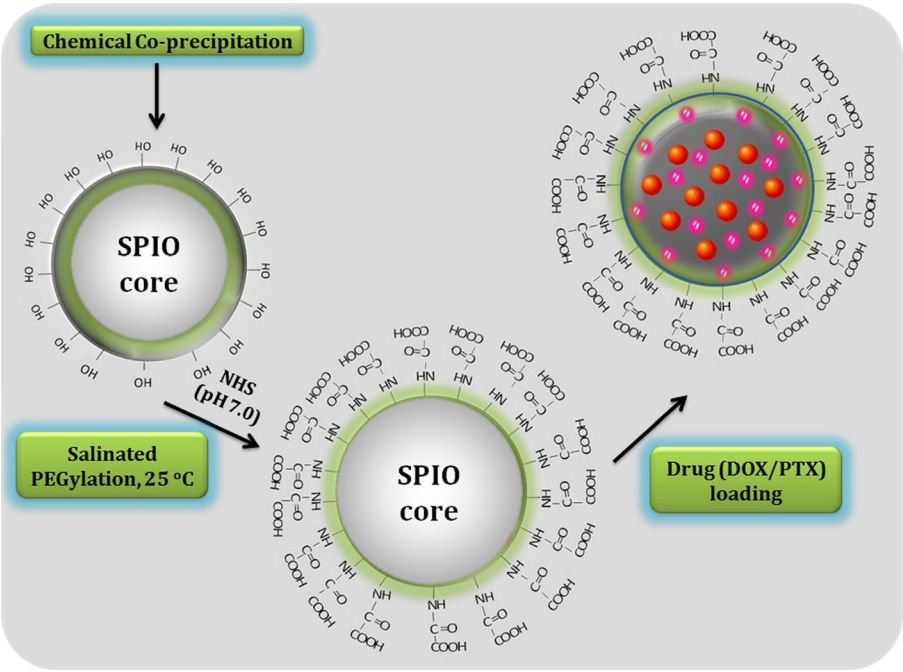

Fig. 3 The schematic cutaway for the method of SPIO NP synthesis by controlled chemical coprecipitation method and their modification with APTES–PEG and drug loading via oil-in-emulsion method

Surface Morphology of Drug-Loaded AP-SPIO NPs

Figure 3 demonstrates the schematic diagram of the synthesis of surface modified and drug (DOX/PTX)-loaded SPIO NPs. Morphological properties of unmodified, AP-modified, DOX-AP-SPIO NPs, and PTX-AP-SPIO NPs were evaluated by SEM, as shown in Fig. 4a–d, respectively. The SEM micrographs demonstrate that the AP-SPIO NP complex was largely composed of nearly globular structures of various sizes, dispersed throughout the matrix (Fig. 4b). The mean diameter of the AP-SPIO NP's globular structures was estimated to be about 17 nm while, after drug loading, the dispersed and spherical structures were seen with slightly increased particle size (27±0.7 and 30±0.45 nm) for the PTX- and DOX-AP-SPIO NPs, respectively (Fig. 4c, d).

In Vitro Drug Loading and Release Profiles for AP-SPIO NPs

Drug loading capacity (w/w %) of AP-SPIO NPs was evaluated separately by using calibration curves, made by reading separate absorptions of 1–250 μM (0.1–10 μg/g) DOX and PTX by UV-visible spectrophotometry (200–800 nm) at room temperature. According to Fig. 4e, the percentage of loaded DOX and PTX increased with increasing their initial amounts and reached a maximum of 70 and 61.5 % for 250 μM (10 μg) DOX and PTX ($p<0.001$), respectively [19]. The amounts of loaded DOX and PTX were 35 and 30.75 μg/g SPIO NPs.

The amount of drug release from AP-SPIO NPs was assessed in vitro. According to Fig. 4f, the release of DOX and PTX was 49 and 54 % from unmodified SPIO NP

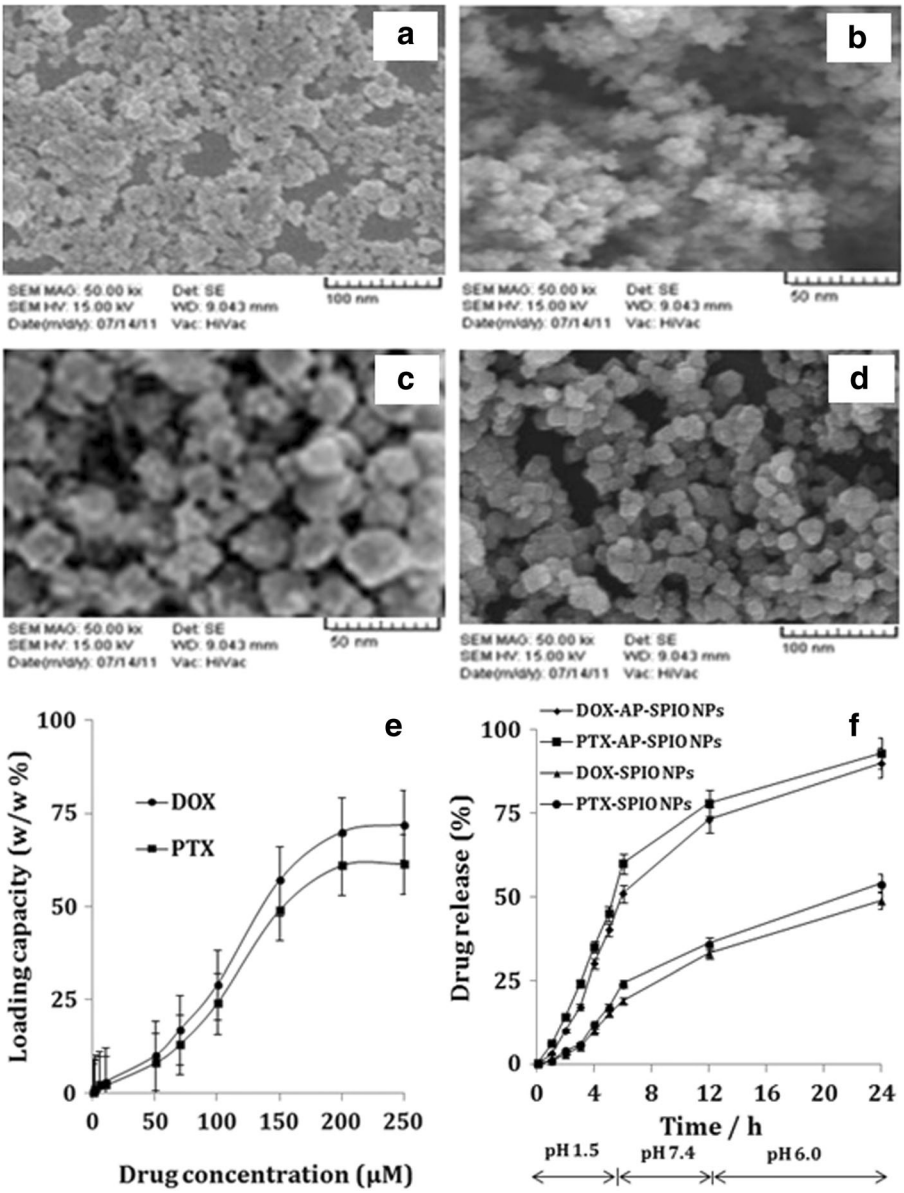

Fig. 4 The diameters of **a** unmodified, **b** AP-SPIO NPs, **c** PTX-AP-SPIO NPs, and **d** DOX-AP-SPIO NPs were evaluated via SEM, and the resulting micrographs were measured by comparing them with the scale bar. **e** Quantification of DOX and PTX (1–250 μM in PBS) loading into AP-SPIO NP core. Amount of loaded/remaining drug was determined by UV-visible spectrophotometry (λ=200-800 nm). **f** In vitro drug release profiles of DOX and PTX from AP-SPIO NPs at different pH values (1.5-7.4) at room temperature (n=3)

core, respectively, while DOX and PTX, loaded inside the AP-SPIO core, showed significant and sustained release (90 and 93 %) at pH 6.0, respectively. This is a desirable condition for a tumor microenvironment with prevalent acidic pH. The diffusion and sustained release of nanocomposite-based antineoplastic agents can be

related to the influence of concentration gradient, which is similar to the previous observation [20]. In our study, a small amount of drug release was observed at pH 7.4 after 24 h. This is a desirable characteristic, as the physiological pH is undesired for proper release of drugs from nanocomposite-based drug delivery vehicles. This pH-dependent drug release behavior is favorable for the chemotherapeutic process, as it can significantly reduce the premature drug release and harm to normal tissues at physiological pH (pH 7.4) while maximizing the amount of drug reaching the target tumor cells by passive targeting [21]. Thus, our formulation offered sustained release of antineoplastic agents of two different origins, from the AP-SPIO NPs at the physiological pH, which is an essential requirement of cancer therapy.

Uptake and Cytotoxicity of Drug-Loaded AP-SPIO NPs in Ovarian Cancer Cells

Cytotoxicity in the cultured A2780 and OVCAR-3 cells was determined using MTT assay. The incorporation of PTX and DOX into AP-SPIO core strongly enhanced the cytotoxic effect of drug as compared to the free drug, which is more significant for prolonged incubation times. Figure 5a, b demonstrates the effect of different concentrations (0.1–10 μg/ml NP) of DOX and PTX on the viability of A2780 and OVCAR-3 cells. The cell viability was 3 and 12 % in A2780 cells after 24 h of incubation with 10 μg/ml PTX-AP-SPIO NPs and DOX-AP-SPIO NPs, respectively, which shows significant antineoplastic effect as compared to free drugs ($p<0.001$; Fig. 5a) while OVCAR-3 survival reached up to 10 and 21 % when treated separately with 10 μg/ml PTX-AP-SPIO NPs and DOX-AP-SPIO NPs, respectively ($p<0.001$, Fig. 5b) [22, 23]. Time-dependent drug release and antineoplastic effect were also carried out for 12–96 h. Half the volume of culture media was replaced every 12 h with serum-free media to "starve" the cells, allowing for an enhanced uptake of nanoconjugates. According to Fig. 5c, d, the amount of A2780 and VCAR-3 cell-proliferation reached up to 9, 15, 17, and 29 % in the presence of DOX-AP-SPIO NPs and PTX-AP-SPIO NPs after 96 h, respectively ($p<0.001$) [24]. These results show that as compared with free drugs, their same amounts, loaded in AP-SPIO nanocomposites, had significantly better effects.

Flow Cytometry and Confocal Microscopy

The apoptosis-inducing effect of free DOX, free PTX, DOX-AP-SPIO, and PTX-AP-SPIO NPs was evaluated in A2780 and OVCAR-3 cells by annexin V-FITC and PI double staining. Flow cytometry was used to determine the proportion of live and apoptotic cells. As shown in Fig. 6a, 10 μg/ml DOX-AP-SPIO NPs caused a significant amount of apoptosis (84.4 and 80.84 %) in A2780 and OVCAR-3 cells as compared with the free drugs and control group ($p<0.001$), respectively, while PTX-AP-SPIO NPs caused 75.4 and 74.65 % apoptosis in A2780 and OVCAR-3 cells, respectively ($p<0.001$). Figure 6b demonstrates the bright-field phase contrast photographs of A2780 and OVCAR-3 cells, administered with PTX, DOX, DOX-AP-SPIO, and PTX-AP-SPIO NPs for 48 h.

Analysis of Protein Expression

To better understand the up- and downregulation of cytoplasmic and mitochondrial gene products, the expression of proapoptotic protein bax, antiapoptotic proteins bcl-2, and survivin, and transcriptional regulation factor NF-κB was evaluated in A2780 and

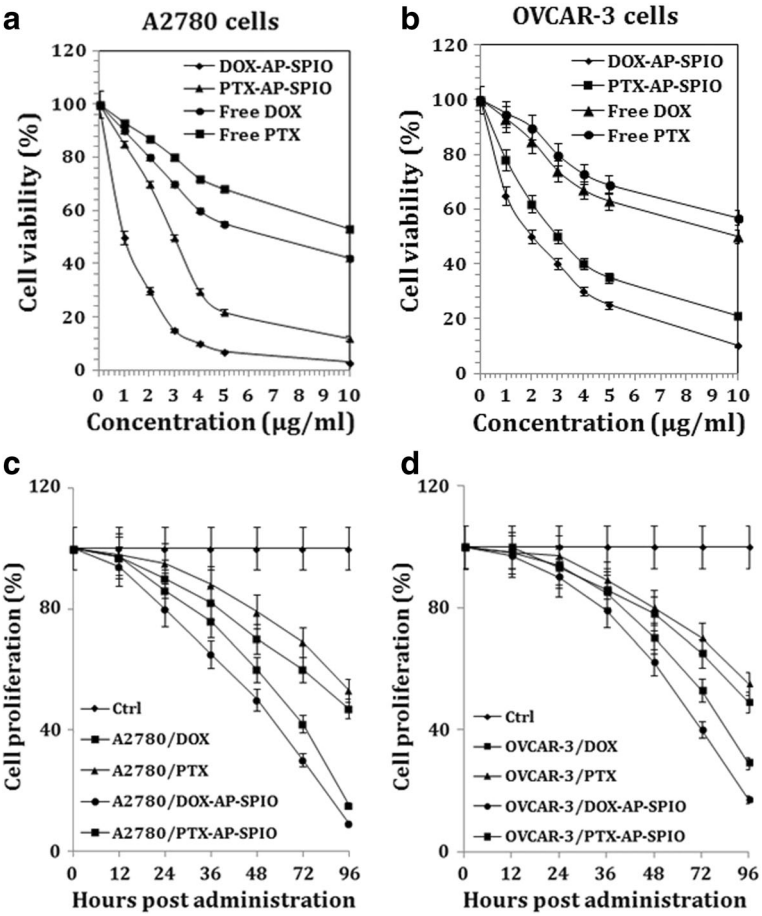

Fig. 5 MTT assay of 0.1–10-μg/ml DOX-AP-SPIO and PTX-AP-SPIO NPs' cytotoxicity in A2780 and OVCAR-3 cells after 48 h. **c** and **d** Inhibition of cell proliferation was also evaluated via MTT assay with the most effective drug concentration (DOX/PTX=10 μg/ml) in the same experimental groups, for the incubation periods of 12, 24, 36, 48, 72, and 96-h post incubation (mean±SD of n=3; p<0.001vs the control group)

OVCAR-3 cells, treated with 10 μg/ml DOX, PTX, DOX-AP-SPIO, and PTX-AP-SPIO NPs, respectively. According to Fig. 7a, b, the NF-κB and bax showed high expression, causing significant amount of apoptosis in both cancer cell lines (p<0.001) while bcl-2 and survivin proteins had a sharp decrease in both cell lines, treated with DOX-AP-SPIO and PTX-AP-SPIO NPs [25]. Figure 7c, d shows the graphical representation for relative activity of pro- and antiapoptotic proteins in A2780 and OVCAR-3 cell lines. This represents the activation of apoptotic mechanism after the nanoparticulate drug delivery in vitro (p<0.001).

Antineoplastic Effect of Drug-Loaded Nanocomposites In Vivo

Different groups of immune-deficient female Balb/c mice (n=12) were peritoneally injected with 200 μl of either of the A2780 or OVCAR-3 cells into the bursa. The animals were kept for 30 days

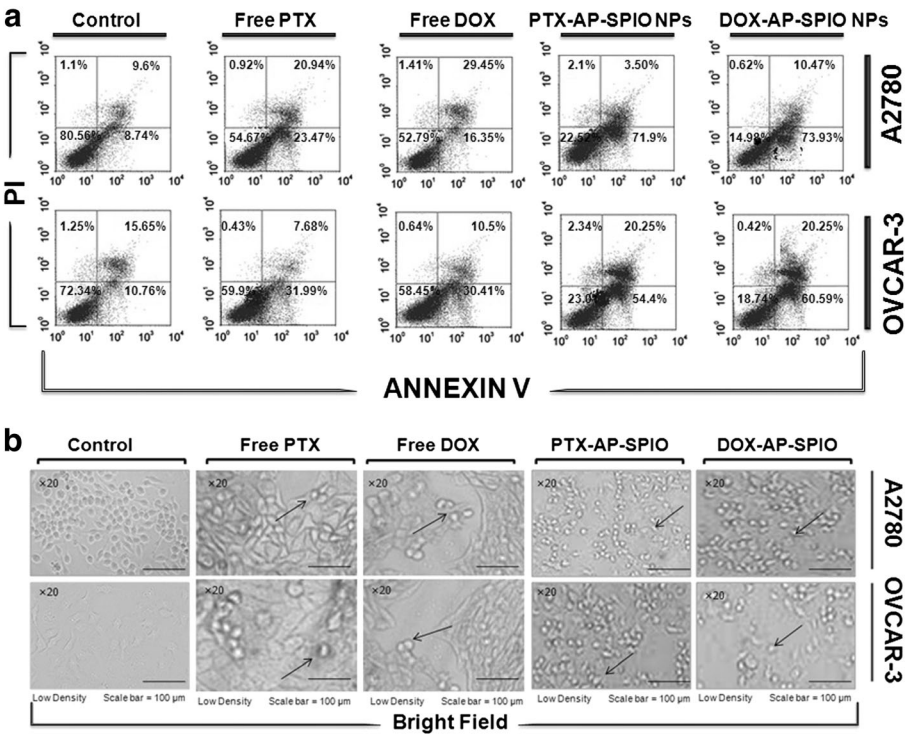

Fig. 6 The apoptotic-inducing effect of free DOX, free PTX, DOX-AP-SPIO, and PTX-AP-SPIO NPs in A2780 and OVCAR-3 cells. Fluorescein-isothiocyanate-labeled annexin V (annexin V-FITC) and propidium (PI) double staining and flow cytometry were used to determine the proportion of live cells (annexin V-FITC and PI double negative, *bottom left quadrant*), early apoptotic cells (annexin V-FITC and PI negative, *bottom right quadrant*), late apoptotic cells (annexin V-FITC and PI positive, *top* left quadrant), and necrotic cells (annexin V-FITC and PI double positive, *top right quadrant*). **b** Bright-field phase contrast photographs of A2780 and OVCAR-3 cells administered with (10 μg/ml drug) free PTX, free DOX, DOX-AP-SPIO, and PTX-AP-SPIO NPs for 48 h

under normal conditions to leave the cells undergo tumorigenesis. Three mice of every group were dissected to calculate the mean tumor volume, which was recorded to be about 2,920 mm^3 after 7 days. Intraperitoneal carcinoma, ovarian carcinoma, and ascites were produced in most of the mice. The mice with ovarian cancer were selected for histological examination of normal (control group) and cancerous ovarian tissues. Figure 8a–h shows that the ovarian tissues of the mice were normal after 7 days of cancer-cell inoculation, but after 25 and 40 days of inoculation, the cancer arose in the ovarian tissue and peritoneum. Histological analysis revealed substantial differences in cell shape, size, and distribution between normal and cancerous ovarian tissue of the mice model [26].

After 30 days, the cancerous mice were inoculated with 200 μl of DOX, PTX, DOX-AP-SPIO NPs, and PTX-AP-SPIO NPs in different groups (n=12) and kept again for 40 days. Animal survival was checked for the entire experimental period. As shown in Fig. 8i, the administration of nanocomposite-based drug delivery increased the survival time and as compared with control, after DOX-AP-SPIO and PTX-AP-SPIO NP administration for 40 days; none of the mice died. After every week, the mice were dissected after 40 days. According to the photographs of Fig. 8j, m, the tumor volume did not change 7 days after administration of

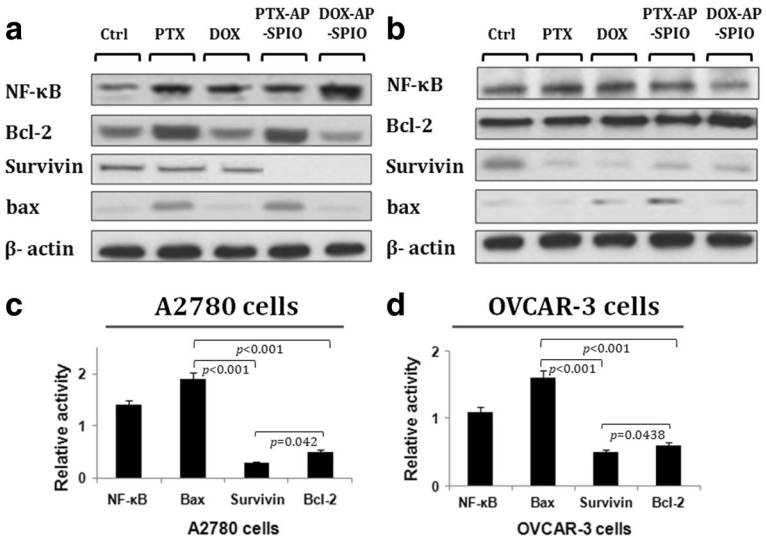

Fig. 7 Western analysis of the effects of free and nanoconjugated (10 μg/ml) DOX and PTX on the expression of survivin, NF-κB, Bcl-2, and bax proteins in **a** A2780 and **b** OVCAR-3 cells. The cancer cells were incubated with 10 μg/ml of DOX, PTX, DOX-AP-SPIO, and PTX-AP-SPIO NPs for 24 h. As a control for loading, the blots were incubated with β-actin antibody. **c** and **d** Graphical representations of the relative activity of the experimental gene products, studied by Western blot analysis (n=3; p<0.001)

free or nanoconjugated drugs (as all experiments showed similar results, only four representative photographs are shown here, p=0.043) while tumor volume shrank to 2,155, 1,015, and 143 mm^3 after 15, 25, and 40 days of the nanocomposite inoculation (p<0.001, Fig. 8l–n). Normal ovarian cells proliferated in an ordered fashion and were elongated or spindle-like in shape, reminiscent of the typical flattened fibroblast-like morphology while cancerous cells had large, nonhomogeneous, and disordered nuclei random pattern and were rounded in shape. Cell density was significantly higher in normal cells (Fig. 8a, e) than in tumor specimens.

Ovarian cancer is among the deadliest carcinomas, and there is an urgent need for a better therapy. Therapies for ovarian cancer fail because they either do not respond to initial therapy or develop recurrent disease. There has been great progress in the development of nanocomposite-based drug delivery systems for cancer therapy [27, 28]. AP-coated SPIO NPs were synthesized to reduce or minimize the undesired interactions or nonspecific uptake of anticancer drugs by normal sites. Biocompatible AP-SPIO nanocarriers were developed for targeted delivery of DOX and PTX, wherein the amount and site of drug release were controlled by the structure of polymer-coated NPs and pH. The present nanocomposites can be used for targeting a broad range of solid tumors such as epithelial ovarian tumor [29, 30]. TEM and XRD size estimates of the NPs were well below the size limit for superparamagnetic behavior (20–25 nm) of magnetite [31].

In this work, DOX- and PTX-encapsulated AP-SPIO NPs were formulated using the oil-in-emulsion (w/o/w) technique [32]. However, the influence of other factors on entrapment efficiency is very complicated and includes polymer concentration, volume of inner and outer aqueous phase, and drug concentration inside the nanocomposites [33]. The loading efficiency values achieved for DOX and PTX were different inside the AP-SPIO NPs, the mechanism of

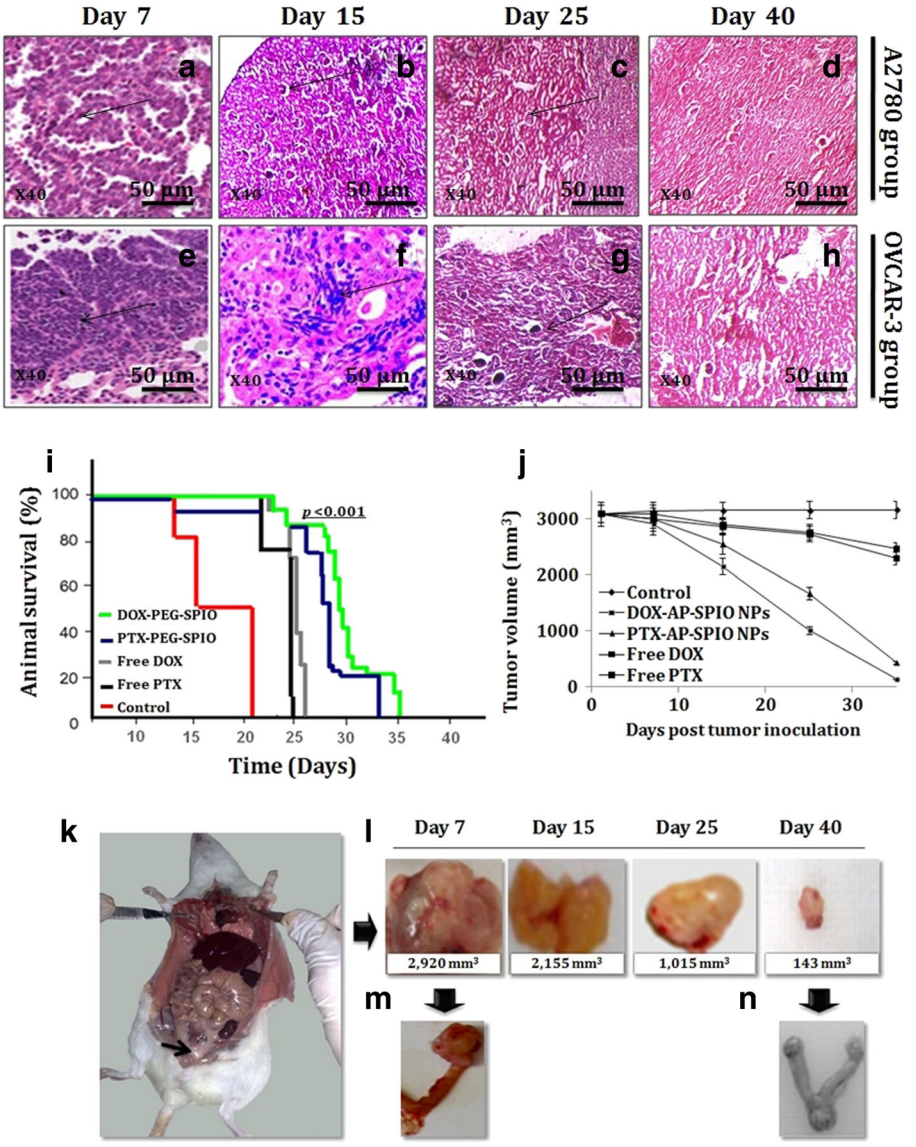

Fig. 8 Histology of the ovarian tissue of BALB/c mice in which the epithelial ovarian tumor was originated. *Photographs* (**a**–**h**) are the sections of ovarian tissue, stained with hemotoxylin and eosin (H&E). *Photographs* **a** and **e** (control) show normal tissue. **Photographs* (**b**–**d**; magnification ×400) show mice ovarian tissue, 7, 15, 25, and 40 days after inoculation of 200 µl of A2780 cells. ***Photographs* (**f**–**h**; magnification ×400) show the mice ovarian tissue 7, 15, 25, and 40 days after inoculation of OVCAR-3 cells. *Photographs* * and ** show magnification clusters of tumor cells with lymphocytic infiltration along with the fibrous connective tissues. i Animal survival curves 0–40 days after the administration of 10 µg/ml free DOX, free PTX, DOX-AP-SPIO, and PTX-AP-SPIO NPs ($p<0.001$). j Estimation of tumor volume, 40 days post administration of free and NP-based drugs. Representative *photographs* (**k** through **n**) show the anticancer effect of drug-loaded nanocomposite systems

which is indistinct. Compared with DOX-AP-SPIO NPs, PTX-AP-SPIO NPs showed a marked decrease in encapsulation efficiency. The entrapment efficiencies of DOX and PTX were 70 (35 μg/g DOX) and 61.5 % (30.75 μg/g PTX) with the particle size of about 30±0.45 and 27±0.7 nm, respectively. The results demonstrated that both drug-loaded NPs showed pH sensitivity and can be applied as an effective carrier for anticancer drugs. It is expected that at acidic tumor pH, these modified drug-loaded NPs can show enhanced cytotoxicity, as compared with those at normal pH [34, 35].

It is generally assumed that drug release occurs by several processes, including diffusion through the polymer matrix, release through polymer degradation and solubilization, and diffusion through microchannels existing in polymer matrix or through the channels that are formed by polymer erosion. Within about 24 h, the drug release from unmodified SPIO NPs was estimated to be 49 and 54 % while 90 and 93 % drug release was observed for DOX-AP-SPIO NPs and PTX-AP-SPIO NPs at pH 6.0, respectively. The drug release occurred through diffusion mechanism after degradation of AP-SPIO NPs within tumors' acidic microenvironment [29].

A2780 and OVCAR3 cell lines showed significant apoptosis when treated with nanocomposite-based drugs. This is consistent with findings in other tumor types [36]. Our study indicates that epithelial ovarian cancer cells are heterogeneous and show different levels of resistance to same drugs. A2780 (3 and 12 % survival) was more sensitive to DOX-AP-SPIO and PTX-AP-SPIO NPs as compared with OVCAR-3 cells (10 and 21 % survival). OVCAR-3 cells have a striking capacity to proliferate, differentiate, and undergo self-renewal, enabling them to eventuate in tumor formation and repopulate tumors after therapy.

In human ovarian cancers, resistance to drug therapy has been often associated to the upregulation of antiapoptotic Bcl-2 and/or Bcl-xL proteins [37]. Less is known about the role of bax (proapoptotic protein) in the development of chemotherapeutic resistance in ovarian cancers, and overexpression of bax has been shown to sensitize ovarian cancer cell lines to drug-mediated apoptosis. During the present study, the newly formulated nanocomposite-based drug delivery system successfully upregulated the bax expression, while downregulating the Bcl-2 and survivin protein expressions. These results are in line with the previous reports [38, 39].

In vivo drug targeting for 40 days showed least side effects on the survival of mice models while tumors of all the control mice were very large, causing ulceration and animal distress and thus commanding euthanasia. The weights of the excised tumors showed that none of the treated mice had tumors large enough to require euthanasia; these mice were killed for the sole reason of comparing the weights and sizes of tumors with those of the untreated group. Tumor size in the treated mice continued to decrease after the administration of nanocomposite-based drugs [40]. These results demonstrate that DOX-AP-SPIO and PTX-AP-SPIO NPs were able to efficiently enter the cells in vivo and specifically target cancer cells and not healthy tissues.

Conclusions

SPIO NPs were prepared using an improved chemical coprecipitation method, and then, AP polymer was used to encapsulate SPIO NPs by an oil-in-emulsion method (w/o/w). The results indicate that the AP-SPIO NPs effectively encapsulated anticancer drugs DOX and PTX.

Acknowledgments The authors are grateful for the financial support of the Research Council of the University of Tehran, Tehran, Iran, to this work.

References

1. Jeun, M., Lee, S., Kang, J. K., Tomitaka, A., & Kang, K. W. (2012). Physical limits of pure superparamagnetic Fe_3O_4 nanoparticles for a local hyperthermia agent in nanomedicine. *Applied Physics Letters, 100*, 092406.
2. Salehizadeh, H., Hekmatian, H., Sadeghi, M., & Kennedy, K. (2012). Synthesis and characterization of core-shell Fe_3O_4-gold-chitosan nanostructure. *Journal of Nanobiotechnology, 10*, 3–9.
3. Cai, H., Xu, C., He, P., & Fang, Y. (2001). Nanoparticles: from theory to applications. *Electroanalytical Chemistry, 510*, 78–85.
4. Wu, W., & Jiang, X. (2012). Long-circulating polymeric drug nanocarriers. Functional nanoparticles for bioanalysis, nanomedicine, and bioelectronic devices. Volume 2, ACS Symposium Series, Vol. 1113, ISBN: 9780841228283, Chapter 2, pp 27–36. 4, 5.
5. Sun, C., Jerry, S., Lee, H., & Zhang, M. (2008). Magnetic nanoparticles in MR imaging and drug delivery. *Advanced Drug Delivery Reviews, 60*, 1252–1265.
6. Neuberger, T., Schopf, B., Hofmann, H., Hofmann, H., & von Rechenberg, B. (2005). Superparamagnetic nanoparticles for biomedical applications: Possibilities and limitations of a new drug delivery system. *Journal of Magnetism and Magnetic Materials, 293*, 483–496.
7. Torchilin, V. P. (2006). Multifunctional nanocarriers. *Advanced Drug Delivery Reviews, 58*, 1532–1555.
8. Zhang, G., Lai, B. B., Zhou, Y. Y., Chen, B. A., & Wang, A. M. (2011). Fe_3O_4 nanoparticles with daunorubicin induce apoptosis through caspase 8-PARP pathway and inhibit K562 leukemia cell-induced tumor growth in vivo. *Nanomedicine: Nanotechnology, Biology, and Medicine, 7*, 595–603.
9. Biranwar, Y. A., Bare, K. R., Mahajan, V. R., Sapate, M. K., & Baviskar, D. T. (2011). Erythrocyte drug delivery system. *International Journal of Pharmaceutical Science Review and Research, 8*, 124–128.
10. Inui, O., Teramura, Y., & Iwata, H. (2010). Retention dynamics of amphiphilic polymers PEG-lipids and PVA-Alkyl on the cell surface. *ACS Applied Material Interfaces, 2*, 1514–1520.
11. Chao, Y., Su, A., Lin, Y., Hsu, W., & Huang, K. (2011). Synthesis and application of polyethylene glycol/vinyltriethoxy silane (PEG/VTES) copolymers. *African Journal of Biotechnology, 10*, 12754–12761.
12. Kitagawa, K., Kubota, K., Sueyoshi, K., & Otsuka, O. (2010). One-step preparation of amino-PEG modified poly(methyl methacrylate) microchips for electrophoretic separation of biomolecules. *Journal of Pharmaceutical Biomedicine and Analysis, 53*, 1272–1277.
13. Cole, A. J., David, A. E., Wang, J., Galbán, C. J., Hill, H. L., & Yang, V. C. (2011). Polyethylene glycol modified, cross-linked starch coated iron oxide nanoparticles for enhanced magnetic tumor targeting. *Biomaterials, 32*, 2183–2193.
14. Xie, J., Xu, C., Kohler, N., Hou, Y., & Sun, S. (2007). Controlled PEGylation of monodisperse Fe_3O_4 nanoparticles for reduced non-specific uptake by macrophage cells. *Advanced Materials, 19*, 3163–3166.
15. Zhang, Y., Kohler, N., & Zhang, M. (2002). Surface modification of superparamagnetic magnetite nanoparticles and their intracellular uptake. *Biomaterials, 23*, 1553–1561.
16. Yue-Jian, C., Juan, T., Fei, X., Jia-Bi, Z., Ning, G., & Yi-Hua, Z. (2010). Synthesis, self-assembly, and characterization of PEG-coated iron oxide nanoparticles as potential MRI contrast agent. *Drug Development and Industrial Pharmacy, 36*, 1235–1244.
17. Chen, Y. J., Tao, J., Xiong, F., Zhu, J. B., Gu, N., & Geng, K. K. (2010). Characterization and in vitro cellular uptake of PEG coated iron oxide nanoparticles as MRI contrast agent. *Pharmazie, 65*, 481–486.
18. Mikhayaylvo, M., Kim, D. K., & Berry, C. C. (2004). BSA immobilization on amine functionalized superparamagnetic iron oxide nanoparticles. *Chemical Materials, 16*, 2344–2354.
19. Naseri, G. M. (2012). The amounts of loaded DOX and PTX were 35 and 30.75 mg/g SPIO NPs. *Carbohydrate Polymers, 90*, 1265–1272.
20. Jain, K. K. (2005). The role of nanobiotechnology in drug discovery. *Drug Discovery Today, 10*, 1435–1442.
21. Wang, H., Shrestha, T. B., Basel, M. T., Dani, R. K., Seo, G., & Balivada, S. (2012). Magnetic-Fe/Fe_3O_4-nanoparticle-bound SN38 as carboxylesterase-cleavable prodrug for the delivery to tumors within monocytes/macrophages. *Beilstein Journal of Nanotechnology, 3*, 444–455.
22. Mahmoudi, M., Simchi, A., Imani, M., Milani, A. S., & Stroeve, P. (2009). An in vitro study of bare and poly(ethylene glycol)-co-fumarate-coated superparamagnetic iron oxide nanoparticles: a new toxicity identification procedure. *Nanotechnology, 20*, 225104.
23. Fonseca, C., Simoes, S., & Gaspar, R. (2002). Paclitaxel-loaded PLGA nanoparticles: preparation, physicochemical characterization and in vitro anti-tumoral activity. *Journal of Controlled Release, 82*, 273–286.
24. Wang, Q., Zheng, X., Yang, L., Shi, Y., Gao, L., & Zhong, L. (2010). Reactive oxygen species-mediated apoptosis contributes to chemosensitization effect of saikosaponins on cisplatin-induced cytotoxicity in cancer cells. *Journal of Experimental and Clinical Cancer Research, 29*, 159–167.

25. Lane, D., Côté, M., & Grondin, R. (2006). Acquired resistance to TRAIL-induced apoptosis in human ovarian cancer cells is conferred by increased turnover of mature caspase-3. *Molecular Cancer Therapy, 5*, 509–521.
26. Vanderhyden, B. C., Shaw, T. J., & Ethier, J. (2003). Animal models of ovarian cancer. *Reproductive Biology and Endocrinology, 1*, 67–77.
27. Ferrari, M. (2005). Cancer nanotechnology: opportunities and challenges. *Nature Reviews Cancer, 5*, 161–171.
28. Pardakhty, A., & Moazeni, E. (2013). Nano-niosomes in drug, vaccine and gene delivery: a rapid overview. *Nanomedicine Journal, 1*, 1–13.
29. Akbarzadeh, A., Mikaeili, H., Zarghami, N., Rahmati, M., Barkhordari, A., & Davaran, S. (2012). Preparation and in vitro evaluation of doxorubicin-loaded Fe_3O_4 magnetic nanoparticles modified with biocompatible copolymers. *International Journal of Nanomedicine, 7*, 144–156.
30. Brullot, W., Reddy, N. K., Wouters, J., Valev, V. K., Goderis, B., & Vermant, J. (2012). Versatile ferrofluids based on polyethylene glycol coated iron oxide nanoparticles. *Journal of Magnetism and Magnetic Materials, 324*, 1919–1925.
31. Gubin, S. P. (2009). *Magnetic Nanoparticles*. Hoboken: Wiley.
32. Sah, H. (1999). Stabilization of protein against methylene chloride water interface-induced denaturation and aggregation. *Journal of Controlled Release, 58*, 143–151.
33. Yoo, H. S., & Park, T. G. (2000). In vitro and in vivo anti-tumor activities of nanoparticles based on doxorubicin-PLGA conjugates. *Journal of Controlled Release, 68*, 419–431.
34. Lu, A. H., Salabas, E. L., & Schuth, F. (2007). Magnetic nanoparticles: Synthesis, protection, functionalization, and application. *Angewandte Chemie International Edition, 46*, 1222–1244.
35. Wang, L. Y., Bai, J. W., Li, Y. J., & Huang, Y. (2008). Multifunctional nanoparticles displaying magnetization and near-IR absorption. *Angewandte Chemie International Edition, 47*, 2439–2442.
36. Hu, L., McArthur, C., & Jaffe, R. B. (2010). Ovarian cancer stem-like side-population cells are tumourigenic and chemoresistant. *British Journal of Cancer, 102*, 1276–1283.
37. Tsuruta, Y., Mandai, M., & Konishi, I. (2001). Combination effect of adenovirus-mediated pro-apoptotic bax gene transfer with cisplatin or paclitaxel treatment in ovarian cancer cell lines. *European Journal of Cancer, 37*, 531–541.
38. Muscolini, M., Cianfrocca, R., & Sajeva, A. (2008). Trichostatin A up-regulates p73 and induces Bax-dependent apoptosis in cisplatin-resistant ovarian cancer cells. *Molecular Cancer Therapeutics, 7*, 1410–1419.
39. Villedieu, M., Louis, M. H., & Dutoit, S. (2007). Absence of Bcl-xL downregulation in response to cisplatin is associated with chemoresistance in ovarian carcinoma cells. *Gynecologic Oncology, 105*, 31–44.
40. Hine, C. M., Seluanov, A., & Gorbunova, V. (2012). Rad51 promoter-targeted gene therapy is effective for in vivo visualization and treatment of cancer. *Molecular Therapy, 20*, 347–355.